Su, Z.-K., Zhao, X.-F., Wang, C.Y., Zi, J.-W., McNaughton, N.J., and Spandler, C., 2023, Hydrothermal alteration episodes reflect multiple Proterozoic tectonic and magmatic events in the Kangdian region, western Yangtze Block: GSA Bulletin, https://doi.org/10.1130/B36542.1.

Supplemental Material

Supplementary Text S1. Analytical methods.

Figure S1. Geologic cross section of No. 30 exploration line of Dahongshan deposit, showing spatial relationship between intensely metasomatic rocks and Fe-Cu orebodies.

Figure S2. Plots of major element compositions of allanite in metasomatic or mineralized rocks in Dahongshan Group, using per formula unit (apfu) and atomic ratio.

Figure S3. Th-U plot displaying contrasting Th and U concentrations among different occurrences of allanite.

Figure S4. Representative LA-ICP-MS down-hole profile of U-Pb isotopic ratios of mixed analyses of monazite I (DHS13-60).

Table S1. Allanite chemical compositions.

Table S2. SHRIMP U-Pb data of allanite.

Table S3. SHRIMP U-Pb data of monazite.

Table S4. LA-ICP-MS U-Pb data of allanite.

Table S5. LA-ICP-MS U-Pb data of monazite.

Table S6. LA-ICP-MS U-Pb data of apatite.

Table S7. LA-ICP-MS U-Pb data of rutile.

Table S8. ID-TIMS Re-Os data of molybdenite.

Table S9. Compilation of available geochronology data for hydrothermal events in Dahongshan Group.

Table S10. References of data sources for Fig. 14 in text.

Supplementary Materials

Supplementary Text S1: Analytical methods

Figure S1. Geologic cross section of No. 30 exploration line of Dahongshan deposit, showing spatial relationship between intensely metasomatic rocks and Fe-Cu orebodies. The bottom solid line represents the bottom of drill holes.

Figure S2. Plots of major element compositions of allanite in metasomatic or mineralized rocks in Dahongshan Group, using per formula unit (apfu) and atomic ratio. (A) La versus Ce showing Ce/La ratio over 1. (B) Al versus ΣLREEs (La + Ce + Pr + Nd) plot with emphasis on core-rim zonation. Note the negative correlation between Al and ΣLREE. (C) Negative correlation between Ca and ΣREEs in all allanite generations representing the dominant substitution of $^{A}LREE^{3+}$ + $^{M}(Fe^{2+}+Mg^{2+})$ for $^{A}Ca^{2+}$ + $^{M}(Al^{3+}+Fe^{3+})$. (D) Negative correlation between $Fe^{3+}/(Fe^{3+}+Fe^{2+})$ and ΣREEs.

Figure S3. Th-U plot displaying contrasting Th and U concentrations among different occurrences of allanite. Note that the core-rim of Aln I is compatible with core domain of Aln II in terms of both chemical compositions and U-Pb ages.

Figure S4. Representative LA-ICP-MS down-hole profile of U-Pb isotopic ratios of mixed analyses of monazite I (DHS13-60). Blue spots denote raw ratios of $^{206}Pb/^{238}U$, red spots are moving averages to better show the trends. Note the stepped $^{206}Pb/^{238}U$ ratios from surface to depth representing traverse from rim2 to rim1, and eventually to the relic core. The Pb/U ratios are raw, labelled with corresponding ages calibrated from strictly time interval-matched integration.

Table S1. Allanite chemical compositions.
Table S2. SHRIMP U-Pb data of allanite.
Table S3. SHRIMP U-Pb data of monazite.
Table S4. LA-ICP-MS U-Pb data of allanite.
Table S5. LA-ICP-MS U-Pb data of monazite.
Table S6. LA-ICP-MS U-Pb data of apatite.
Table S7. LA-ICP-MS U-Pb data of rutile.
Table S8. ID-TIMS Re-Os data of molybdenite.
Table S9. Compilation of available geochronology data for hydrothermal events in Dahongshan Group.
Table S10. References of data sources for Fig. 14 in text.

Supplementary Text S1: Analytical methods

Textural characterization and chemical analysis by SEM and EMPA

Texture characterizations of accessory minerals (apatite, allanite, monazite, and rutile) for in-situ dating were examined by field-emission (FE) scanning electron microscope (SEM) in State Key Laboratory of Geological Processes and Mineral Resources (GPMR), China University of Geosciences, Wuhan. We first use automatic contrast to reveal the textural arrangement and locations of interested accessory minerals within sections. Then the contrast was amplified for all SEM imaging until the potentially subtle zoning of accessory minerals was visually clear, especially for allanite and monazite grains.

Quantitative analyses of allanite and X-ray maps of monazite were performed on a wavelength-dispersive-spectrometry equipped JEOL JXA-8100 electron microscope at the Center for Material Research and Analysis, Wuhan University of Technology. Representative monazite grains were mapped for Th and Y to better reveal the elemental distribution and possible mineral inclusions in different domains. Quantitative analyses of allanite were performed with 15 kV accelerating voltage, 20 nA beam current, and 5 μm beam diameter. The analyzing crystals were TAP (Si, Ti, Mg, Al), PET (Ca, Th, P), and LiF (Fe, Mn, REE). Counting time were adjusted to the element concentrations and varied from 40-70 s. Selected spectral lines include: Kα for Si, Ti, Mg, Al, Ca, P, Fe, and Mn; Lα for La and Ce; Lβ for Pr, Nd, and Sm, and; Mα for Th. Background offsets were based on both sides of the peak for half of the peak time. Standards were almandine (Si and Al), rutile (Ti), olivine (Mg), apatite (Ca and P), monazite (Th), hematite (Fe), rhodonite (Mn), synthetic $LaPO_4$ (La), synthetic $CePO_4$ (Ce), synthetic $PrPO_4$ (Pr), synthetic $NdPO_4$ (Nd), and synthetic $SmPO_4$ (Sm). Data were reduced on-line using a conventional ZAF routine. Full dateset of allanite compositions are listed in Table S1.

SHRIMP U-Pb dating (Allanite+Monazite)

In-situ U-Pb dating of allanite and monazite use the sensitive high-resolution ion microprobe (SHRIMP II) hosted at the John de Laeter center, Curtin University. Detailed analytical procedures of monazite and allanite are similar with those described by Fletcher et al. (2010) and Rasmussen and Fletcher (2010) are outlined briefly here. Reference standards were placed in separate mounts that were cleaned and Au-coated with the sample mounts for each analytical session. Instrument setup for allanite and monazite are similar. The O_2^- primary beam was accelerated at 10 kV with an intensity of 0.2 to 0.5 nA and was focused through 50-μm Kohler aperture onto ~10 μm spots. The post-collector retardation lens was activated to reduce stray ion arrivals. The mass resolution (M/ΔM at 1% peak height) was >5000 in all sessions. Data were collected in a set of 7 scans, with every four to six sample analyses bracketed by analysis of allanite and monazite reference grains. Count times per scan for Pb isotope 204, background, 206, 207, and 208 were 10, 20, 10, 30, and 10s, respectively. The primary monazite reference material for calibration of Pb/U and Pb/Th isotopic ratios was French. Two

other monazite standards Z2908 (1796 Ma) and Z2234 (1024 Ma) were the secondary reference materials used to monitor matrix effects (See details in Fletcher et al., 2010). Z2908 was also used to monitor, and correct for, the instrumental mass fractionation in $^{207}Pb/^{206}Pb$. Ten analyses of monazite standards Z2908 and Z2234 yield weighted mean $^{207}Pb/^{206}Pb$ ages of 1796 ± 5 Ma (1σ) and 1038 ± 21 Ma (1σ), respectively, both matching well with recommended ages. Investigated allanite in this study was analyzed in the same session within those reported in Su et al. (2021). The primary allanite reference material was Tara (420.3 Ma; Gregory et al., 2007; Smye et al., 2014). Two in-house allanite standards, AlBur and AlCal, were the secondary reference materials used to monitor matrix effects. For allanite, references ALBUR and ALCAL yielded 1456 ± 23 Ma (n = 3) and 109.8 ± 2.2 Ma (n = 4), respectively, within uncertainties of the best estimates of 1442 ± 6 Ma and 108.2 ± 1.1 Ma for ALBUR and ALCAL at 1 sigma, respectively (Su et al., 2021). Data were reduced with the program Squid 2.5 (Ludwig, 2009). Common Pb corrections were made using conventional ^{204}Pb method and the two-stage evolution model of Stacey and Kramers (1975). One dimensional calibrations of $^{206}Pb^{+}/^{270}[UO_2]^{+}$ and $^{208}Pb^{+}/^{264}[ThO_2]^{+}$ was used for both monazite and allanite (Fletcher et al., 2010). Corrections for U, Th, Pb, and REE matrix effects in Pb/U and Th/U, and renormalization of $^{207}Pb/^{206}Pb$ data followed Fletcher et al. (2010). The SHRIMP data for allanite and monazite are listed in the Supplemental Materials (Tables S2-S3).

LA-ICP-MS U-Pb dating (Allanite+Monazite+Apatite+Rutile)

In-situ U-Th-Pb geochronology for allanite in sample DHS13-43 (Aln I) were achieved by using a Resonetics M-50 193nm ArF excimer laser ablation system connected with an Agilent 7700x quadrupole ICP-MS located at the Department of Earth Sciences, University of New Brunswick. The detailed analytical set-up and procedure are described in McFarlane (2016). Non-matrix-matched standardization were adopted to minimize the laser-induced elemental fractionation through a combination of low fluence and high crater diameter/depth ratio. The operating conditions in this study consist of 1 J/cm^2 fluence, 3 Hz frequency, 25 s ablation, and 45 μm crater diameter, resulting in 3 ± 1 μm depth ablation pits. NIST610 were used as the primary external standard. Two in-house allanite standard (SISS and Hartfield) were tested as quality control materials. Measured SISS isochrone produce lower intercepts at 32.8 ± 2.3 Ma (anchored $^{207}Pb/^{206}Pb_c$ at 0.8363 ± 0.0002), which overlaps within error of the reported age (31.53 ± 0.36 Ma; von Blackenburg, 1992). The obtained lower intercepts for Hartfield allanite with anchored common-Pb $^{207}Pb/^{206}Pb$ ratios return an age of 406 ± 7 Ma (anchored $^{207}Pb/^{206}Pb_c$ at 0.856 ± 0.004), which is slightly younger than the recommended value of 415 ± 2 Ma for TIMS titanite from the same tonalite (Bevier and Whalen, 1990). This small discrepancy may be ascribed to heterogeneity of Hartfield allanite grains (cf. McFarlane, 2016). Integration of background and analytical signals, and time-drift correction and quantitative calibration for trace elements were undertaken using Iolite 3.64 software (Paton et al., 2011). The LA-ICP-MS age data for allanite I are listed in the Supplemental Material (Table S4).

Integrated U-Pb dating of other allanite samples (DHS13-42 and DHS10-74) were performed on an ASI J200 Tandem QX fs-laser ablation system equipped with an iCAP-RQ ICP-MS at Chinese Academy of Sciences Key laboratory of Mineralogy and Metallogeny, Guangzhou Institution of Geochemistry. The analytical protocol is similar with those for the 193 nm laser ablation system. The operating conditions in this study consist of beam diameter of 40 μm, repetition rate of 6 Hz, and energy percentage of 70. Argon was used as the make-up gas and mixed with helium as the carrier gas via a T-connector before entering the ICP. Nitrogen was added into the central gas flow (Ar + He) of the Ar plasma to decrease the detection limit and improve precision, consequently increasing the sensitivity for most elements by a factor of 2 to 3 (cf. Hu et al., 2008). Each analysis incorporated a background acquisition of 20–30 s (gas blank) followed by 50 s data acquisition. Allanite standard Tera (420.3 Ma; Gregory et al., 2007; Smye et al., 2014) was used as a calibration standard for mass discrimination and U-Th-Pb isotope fractionation. A secondary allanite standard used as quality control is allanite L166 from hydrothermal breccia in Lanniping IOCG deposit in Kangdian, which is characterized by a Paleoproterozoic age, extremely low Th contents but moderate U contents, negligible common Pb contents with $f^{206}Pb_c$ mostly below 1%, and relatively homogeneous Pb compositions among grains. Working values for L166 were calculated from weighted averages of 26 SHRIMP analyses from Su et al. (2021), which consist of $^{207}Pb/^{206}Pb$ (0.1057 ± 0.0011), $^{207}Pb/^{235}U$ (4.25 ± 0.18), and $^{206}Pb/^{238}U$ (0.294 ± 0.011) with all errors propagated at 2σ. Off-line data selection and integration were performed by using Iolite 4 software (Paton et al., 2011). A total of 19 analyses of the L166 in the whole analytical session yields a weighted mean $^{207}Pb/^{206}Pb$ age of 1704 ± 44 Ma, which matches well with the reported age (1719 ± 22 Ma) given by ion probe. The LA-ICP-MS age data for allanite are listed in the Supplemental Material (Table S4).

In-situ U-Th-Pb dating of monazite were conducted in Institute of Geology and Geophysics, Chinese Academy of Sciences (IGG-CAS), using Geolus plus 193 ArF excimer laser plus an Agilent 7500. The detailed analytical set-up and procedure are described in Liu et al. (2012). Trace element were analyzed simultaneously with U-Th-Pb isotope analyses. Analyses were performed with a spot size of 24 or 32 μm and a frequency of 4 Hz. International monazite standard M4 were used to correct U-Th-Pb fractionation and instrumental mass discrimination. Another standard E0013 were used as monitor material. Ten spots on E0013 yield a weighted mean $^{206}Pb/^{238}U$ age of 588 ± 3 Ma, overlap within errors of the reported value of 587 ± 5 Ma (Janasi et al., 2003). The monazite age data are listed in the Supplemental Material (Table S5).

In-situ U-Pb isotopes of apatite and rutile were analyzed using a RESOlution 193 nm laser ablation system coupled to a Thermo iCAP-Q ICP-MS at GPMR. Analytical conditions similar to those reported in Ying et al. (2020). Samples were ablated using a spot size of 90 μm, a repetition rate of 8 Hz, and energy density of 5–6 J/cm^2. The MAD apatite is used as primary reference and Durango apatite is used as monitor standard. Eight analyses of Durango apatite (archored common $^{207}Pb/^{206}Pb_i$ at 0.83771 ± 0.03) yielded weighted average ^{207}Pb-corrected $^{206}Pb/^{238}U$ age of 30.7 ± 2.4 Ma (cf. Chew et al., 2011), in accordance with recommended age of 31.44 ± 0.18 Ma

(McDowell et al., 2005). Off-line data reduction was carried out using Iolite 4. Rutile were separated, handpicked and mounted in epoxy mounts. Operating conditions for rutile are 90 μm diameter, 5 Hz, and 6 J/cm^2. The external standard zircon 91500 was used for calibrating mass discrimination and U–Pb isotope fractionation due to the lack of rutile standards and the diminished matrix-dependent fractionation between zircon and rutile under conditions with large diameter/depth ratio (e.g. Hou et al., 2020). The reproducibility and accuracy of U-Pb dating have been assessed by replicate analyses of a secondary zircon standard GJ-1 (Jackson et al., 2004). Overall analyses of GJ-1 in this analytical session yield a weighted mean $^{206}Pb/^{238}U$ age of 604 ± 6 Ma (n = 3), which is in good agreement with the recommended values (601.86 ± 0.37 Ma at 2σ; Horstwood et al., 2016). Off-line selection and integration of background and analyzed signals, time-drift correction, and quantitative calibration for U-Pb dating were performed using ICPMSDataCal. The age data for apatite and rutile are listed in the Supplemental Material (Tables S6-S7).

ID-N-TIMS Re-Os (Molybdenite)

Molybdenite separation and Re-Os negative thermal ionization mass spectrometry (N-TIMS) dating protocols were deployed at the Source Rock and sulfide geochronology and geochemistry laboratory at Durham University. Detailed analytical procedures followed those in Selby and Creaser (2001). Following conventional molybdenite separation (crushing, heavy liquids separation, and handpicking), molybdenite digestion, Re-Os isolation and extraction, and filament loading, Re-Os isotopes were measured with a Thermo Scientific Triton mass spectrometer in Durham University. Calibration and uncertainties calculations followed those in Li et al. (2016). The Re-Os data are listed in the Supplemental Material (Table S8).

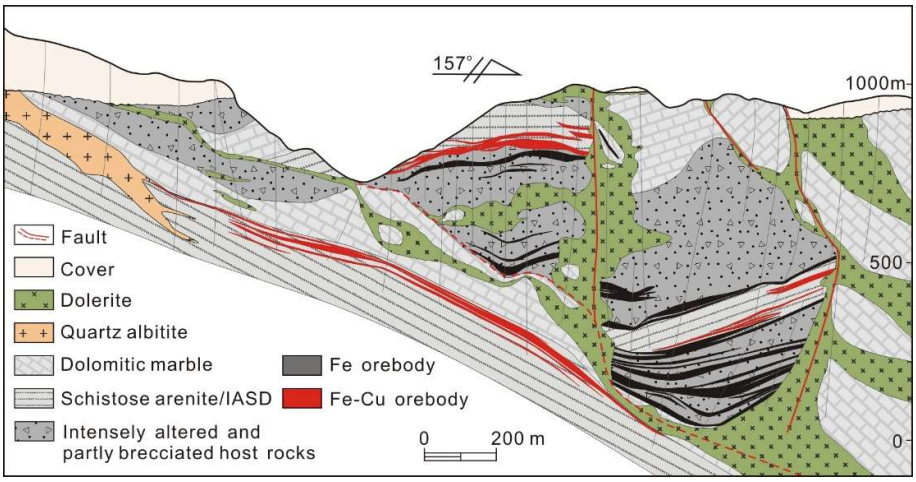

Figure S1. Geologic cross section of No. 30 exploration line of Dahongshan deposit, showing spatial relationship between intensely metasomatic rocks and Fe-Cu orebodies. The bottom solid line represents the bottom of drill holes.

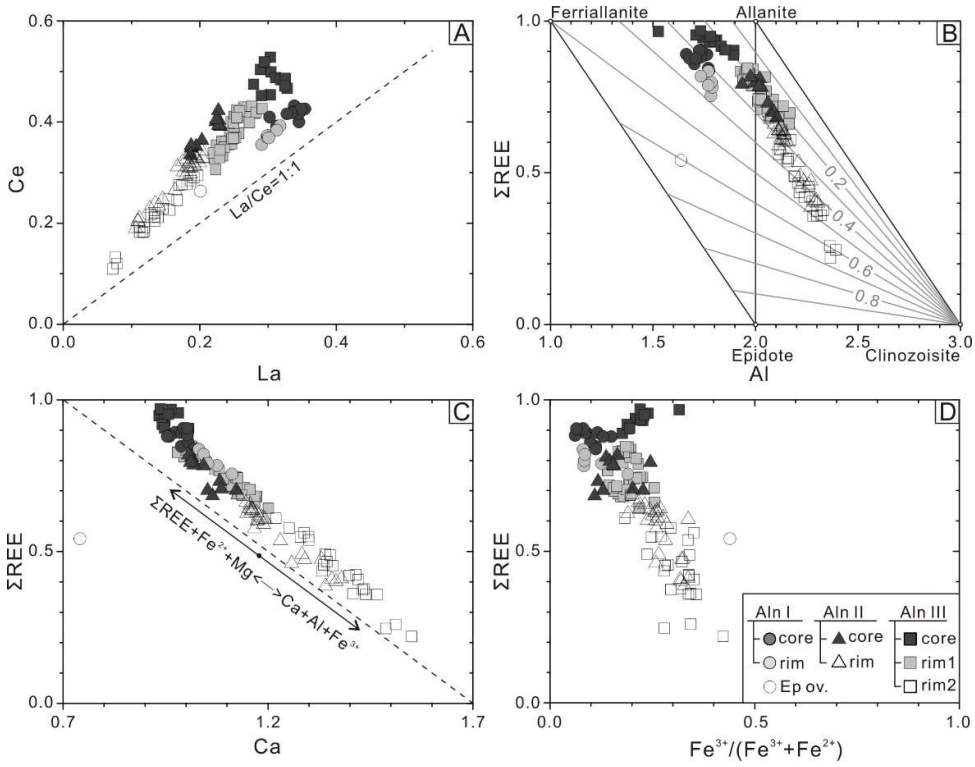

Figure S2. Plots of major element compositions of allanite in metasomatic or mineralized rocks in Dahongshan Group, using per formula unit (apfu) and atomic ratio. (A) La versus Ce showing Ce/La ratio over 1. (B) Al versus ΣLREEs (La + Ce + Pr + Nd) plot with emphasis on core-rim zonation. Note the negative correlation between Al and ΣLREE. (C) Negative correlation between Ca and ΣREEs in all allanite generations representing the dominant substitution of $^{A}LREE^{3+}$ + $^{M}(Fe^{2+}+Mg^{2+})$ for $^{A}Ca^{2+}$ + $^{M}(Al^{3+}+Fe^{3+})$. (D) Negative correlation between $Fe^{3+}/(Fe^{3+}+Fe^{2+})$ and ΣREEs.

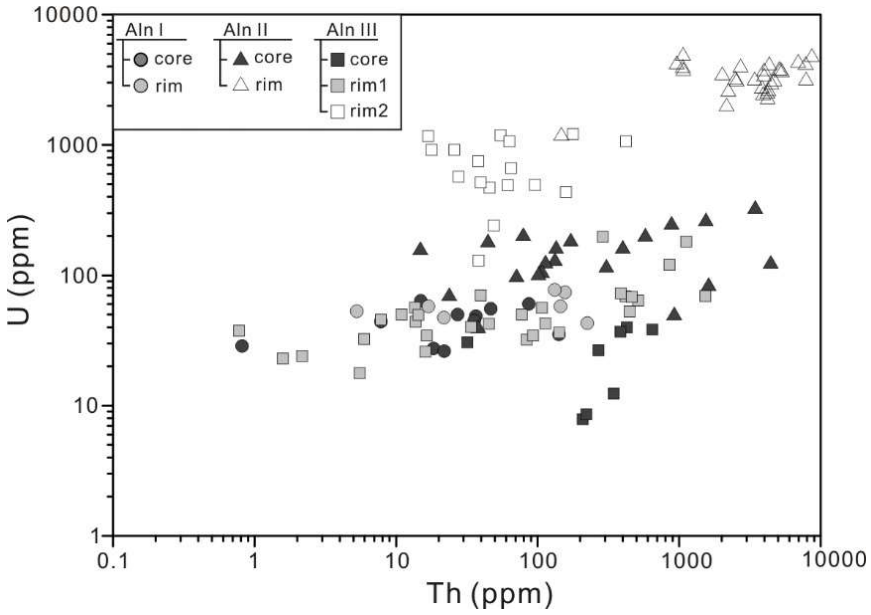

Figure S3. Th-U plot displaying contrasting Th and U concentrations among different occurrences of allanite. Note that the core-rim of Aln I is compatible with core domain of Aln II in terms of both chemical compositions and U-Pb ages.

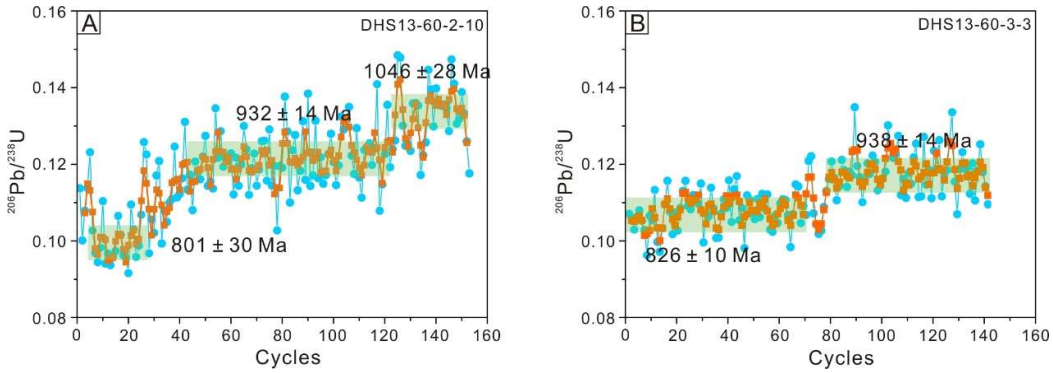

Figure S4. Representative LA-ICP-MS down-hole profile of U-Pb isotopic ratios of mixed analyses of monazite I (DHS13-60). Blue spots denote raw ratios of $^{206}Pb/^{238}U$, red spots are moving averages to better show the trends. Note the stepped $^{206}Pb/^{238}U$ ratios from surface to depth representing traverse from rim2 to rim1, and eventually to the relic core. The Pb/U ratios are raw, labelled with corresponding ages calibrated from strictly time interval-matched integration.

References for analytical methods:

Bevier, M.L., Whalen, J.B., 1990. Tectonic significance of Silurian magmatism in the Canadian Appalachians. Geology, 18(5): 411-414.

Chew, D.M., Sylvester, P.J., Tubrett, M.N., 2011. U–Pb and Th–Pb dating of apatite by LA-ICPMS. Chemical Geology, 280(1-2): 200-216.

Fletcher, I.R., McNaughton, N.J., Davis, W.J., Rasmussen, B., 2010. Matrix effects and calibration limitations in ion probe U–Pb and Th–Pb dating of monazite. Chemical Geology, 270(1-4): 31-44.

Gregory, C.J., Rubatto, D., Allen, C.M., Williams, I.S., Hermann, J., Ireland, T., 2007. Allanite micro-geochronology: A LA-ICP-MS and SHRIMP U–Th–Pb study. Chemical Geology, 245(3-4): 162-182.

Horstwood, M.S.A., Košler, J., Gehrels, G., Jackson, S.E., McLean, N.M., Paton, C., Pearson, N.J., Sircombe, K., Sylvester, P., Vermeesch, P., Bowring, J.F., Condon, D.J., Schoene, B., 2016. Community-Derived Standards for LA-ICP-MS U–(Th–)Pb Geochronology—Uncertainty Propagation, Age Interpretation and Data Reporting. Geostandards and Geoanalytical Research, 40(3): 311-332.

Hou, Z.-H., Xiao, Y.-L., Shen, J., Yu, C.-L., 2020. In situ rutile U-Pb dating based on zircon calibration using LA-ICP-MS, geological applications in the Dabie orogen, China. Journal of Asian Earth Sciences, 192: 104261.

Hu, Z.-C., Gao, S., Liu, Y.-S., Hu, S.-H., Chen, H.-h., Yuan, H.-L., 2008. Signal enhancement in laser ablation ICP-MS by addition of nitrogen in the central channel gas. Journal of Analytical Atomic Spectrometry, 23(8): 1093-1101.

Jackson, S.E., Pearson, N.J., Griffin, W.L., Belousova, E.A., 2004. The application of laser ablation-inductively coupled plasma-mass spectrometry to in situ U–Pb zircon geochronology. Chemical Geology, 211(1-2): 47-69.

Janasi, V.A., Alves, A., Vlach, S.R.F., Leite, R.J., 2003. Granitos peraluminosos da porção central da Faixa Ribeira, Estado de São Paulo: Sucessivos eventos de reciclagem da crosta continental no Neoproterozóico. Geologia USP. Série Científica, 3: 13-24.

Li, Y., Selby, D., Feely, M., Costanzo, A., Li, X.-H., 2016. Fluid inclusion characteristics and molybdenite Re-Os geochronology of the Qulong porphyry copper-molybdenum deposit, Tibet. Mineralium Deposita, 52(2): 137-158.

Liu, Z.-C., Wu, F.-Y., Yang, Y.-H., Yang, J.-H., Wilde, S.A., 2012. Neodymium isotopic compositions of the standard monazites used in U–Th–Pb geochronology. Chemical Geology, 334: 221-239.

Ludwig, K.R., 2009. Squid 2.50, a user's manual: Berkeley, California, USA, Berkeley Geochronology Centre. no.4: 95.

McDowell, F.W., McIntosh, W.C., Farley, K.A., 2005. A precise ^{40}Ar–^{39}Ar reference age for the Durango apatite (U–Th)/He and fission-track dating standard. Chemical Geology, 214(3-4): 249-263.

McFarlane, C.R.M., 2016. Allanite U Pb geochronology by 193 nm LA ICP-MS using NIST610 glass for external calibration. Chemical Geology, 438: 91-102.

Paton, C., Hellstrom, J., Paul, B., Woodhead, J., Hergt, J., 2011. Iolite: Freeware for the visualisation and processing of mass spectrometric data. Journal of Analytical Atomic Spectrometry, 26(12): 2508-2518.

Rasmussen, B., Fletcher, I.R., 2010. Dating sedimentary rocks using in situ U-Pb geochronology of syneruptive zircon in ash-fall tuffs < 1 mm thick. Geology, 38(4): 299-302.

Selby, D., Creaser, R.A., 2001. Re–Os geochronology and systematics in molybdenite from the Endako porphyry molybdenum deposit, British Columbia, Canada. Economic Geology, 96(1): 197-204.

Smye, A.J., Roberts, N.M.W., Condon, D.J., Horstwood, M.S.A., Parrish, R.R., 2014. Characterising the U–Th–Pb systematics of allanite by ID and LA-ICPMS: Implications for geochronology. Geochimica et Cosmochimica Acta, 135: 1-28.

Stacey, J.T., Kramers, J.D., 1975. Approximation of terrestrial lead isotope evolution by a two-stage model. Earth and planetary science letters, 26(2): 207-221.

Su, Z.-K., Zhao, X.-F., Li, X.-C., Zhou, M.-F., Kennedy, A.K., Zi, J.-W., Spandler, C., Yang, Y.-H., 2021. Unraveling mineralization and multistage hydrothermal overprinting histories by integrated in situ U–Pb and Sm–Nd isotopes in a Paleoproterozoic breccia-hosted IOCG deposit, SW China. Economic Geology, 116(7): 1687-1710.

von Blackenburg, F., 1992. Combined high-precision chronometry and geochemical tracing using accessory minerals: applied to the Central-Alpine Bergell intrusion (central Europe). Chemical Geology, 100(1-2): 19-40.

Ying, Y.-C., Chen, W., Simonetti, A., Jiang, S.-Y., Zhao, K.-D., 2020. Significance of hydrothermal reworking for REE mineralization associated with carbonatite: Constraints from in situ trace element and C–Sr isotope study of calcite and apatite from the Miaoya carbonatite complex (China). Geochimica et Cosmochimica Acta, 280: 340-359.